https://doi.org/10.1038/s41565-022-01225-x

Zinc cyclic di-AMP nanoparticles target and suppress tumours via endothelial STING activation and tumour-associated macrophage reinvigoration

Received: 3 November 2021

Accepted: 5 September 2022

Published online: 27 October 2022

Kaiting Yang[1,2,10], Wenbo Han[3,4,10], Xiaomin Jiang[3,10], Andras Piffko[1,2,5], Jason Bugno[1,2,6], Chuanhui Han[7], Sirui Li[8], Hua Liang[1,2], Ziwan Xu[3], Wenxin Zheng[1,2], Liangliang Wang[1,2], Jiaai Wang[1,2], Xiaona Huang[1,2], Jenny P. Y. Ting[8], Yang-Xin Fu[9], Wenbin Lin[1,2,3] ✉ and Ralph R. Weichselbaum[1,2] ✉

The clinical utility of stimulator of interferon genes (STING) agonists has been limited due to poor tumour-targeting and unwanted toxicity following systemic delivery. Here we describe a robust tumour-targeted STING agonist, ZnCDA, formed by the encapsulation of bacterial-derived cyclic dimeric adenosine monophosphate (CDA) in nanoscale coordination polymers. Intravenously injected ZnCDA prolongs CDA circulation and efficiently targets tumours, mediating robust anti-tumour effects in a diverse set of preclinical cancer models at a single dose. Our findings reveal that ZnCDA enhances tumour accumulation by disrupting endothelial cells in the tumour vasculature. ZnCDA preferentially targets tumour-associated macrophages to modulate antigen processing and presentation and subsequent priming of an anti-tumour T-cell response. ZnCDA reinvigorates the anti-tumour activity of both radiotherapy and immune checkpoint inhibitors in immunologically 'cold' pancreatic and glioma tumour models, offering a promising combination strategy for the treatment of intractable human cancers.

The stimulator of interferon genes (STING) plays an important role in DNA sensing to initiate innate immune responses. Pathogen-derived DNA and self-DNA are first sensed by cyclic guanosine monophosphate–adenosine monophosphate (cGAMP) synthase (cGAS), which produces 2′,3′-cGAMP that binds STING in the endoplasmic reticulum and promotes trafficking to the Golgi apparatus[1,2]. STING activation ultimately leads to the induction of type I interferons (IFN-I) and other inflammatory cytokines through the activation of both TANK-binding

[1]Department of Radiation and Cellular Oncology, University of Chicago, Chicago, IL, USA. [2]The Ludwig Center for Metastasis Research, University of Chicago, Chicago, IL, USA. [3]Department of Chemistry, University of Chicago, Chicago, IL, USA. [4]Taiji Group, Chongqing, China. [5]Department of Neurosurgery, University Medical Center Hamburg-Eppendorf, Hamburg, Germany. [6]Committee on Clinical Pharmacology and Pharmacogenomics, University of Chicago, Chicago, IL, USA. [7]Peking University International Cancer Institute, Peking University Cancer Hospital and Institute, Peking University, Beijing, China. [8]Lineberger Comprehensive Cancer Center, Department of Genetics, Department of Microbiology and Immunology, University of North Carolina at Chapel Hill, Chapel Hill, NC, USA. [9]Department of Basic Medical Sciences, School of Medicine, Tsinghua University, Beijing, China. [10]These authors contributed equally: Kaiting Yang, Wenbo Han, Xiaomin Jiang. ✉e-mail: wenbinlin@uchicago.edu; ralph.weichselbaum@uchospitals.edu

kinase 1 (TBK1)/interferon regulatory factor 3 (IRF3) and IκB kinase (IKK)/nuclear factor-kappa B (NF-κB) signalling pathways[3,4]. The STING pathway is critical for the response to multiple cancer treatments and has been implicated in cancer immunity following radiotherapy, targeted therapy and chemotherapy[5–9]. Although the STING pathway presents an attractive therapeutic target, effective systemic delivery remains a challenge. Dimethylxanthone Acetic Acid (DMXAA) exhibited excellent anti-tumour effects in mouse models but failed in a phase III trial[10] and was later found to have no binding affinity towards human STING[11]. Bacterial-derived cyclic dinucleotides (CDNs), such as cyclic dimeric adenosine monophosphate (CDA) and cyclic dimeric guanosine monophosphate, mediate immune responses through both murine and human STING signalling yet have poor bioavailability and stability[12]. The local delivery of CDN derivatives, such as ADU-S100 and MK-1454, has only shown modest clinical responses[4,13], and recent oral and manganese-based formulations have demonstrated some promise for systemic delivery in a limited number of preclinical models[14,15]. There is, therefore, still an unmet need for an efficient, systemic STING agonist delivery system that avoids degradation and targets the tumour microenvironment (TME).

Nanoparticle (NP)-based drug delivery has garnered attention for its ability to improve drug pharmacokinetics, target tumours and reduce side effects[16,17]. Owing to their size, NPs tend to passively accumulate in tumours due to altered vasculature and impaired lymphatic drainage[18]. Nanoscale coordination polymers (NCPs), consisting of a non-toxic zinc phosphate hydrophilic core and surrounding lipid bilayer composed of polyethylene glycol (PEG)-conjugated phospholipids (ZnP), can be loaded with both hydrophilic and hydrophobic moieties and engineered for stimuli-triggered drug release[19], conferring benefits over traditional NP designs. Here we identify a tumour-targeting CDA-loaded NCP (ZnCDA) with potent immunostimulatory properties. Our findings reveal a new mechanism of ZnCDA tumour accumulation, identify a population of ZnCDA-targeted tumour-associated macrophages (TAMs) with potent antigen presentation ability and demonstrate potential therapeutic utility in difficult-to-treat, immunologically 'cold' tumour models that represent incurable human cancers.

Systemic ZnCDA suppresses tumour growth and metastasis

The core–shell ZnCDA was synthesized in a two-step process (Fig. 1a). The CDA-loaded Zn phosphate core was prepared by coordination polymerization of $Zn(NO_3)_2$, sodium phosphate and CDA in a reverse microemulsion and surface capping with the monosodium salt of 1,2-dioleoyl-*sn*-glycero-3-phosphate (DOPA), resulting in monodispersed spherical particles (ZnCDA bare) with a *Z*-average diameter of 47.2 ± 1.3 nm and a polydispersity index (PDI) of 0.15 ± 0.01 (Supplementary Fig. 1a,b). These particles were further coated with a 2:1:1 mixture of 1,2-dioleyl-*sn*-glycero-3-phosphocholine (DOPC), cholesterol and 1,2-diastearoyl-*sn*-glycero-3-phosphoethanolamine-*N*-[amino(polyethylene glycol)$_{2000}$] (DSPE-PEG2000) to form ZnCDA with a diameter of 111.8 ± 0.9 nm and a low PDI of 0.12 ± 0.01 (Fig. 1b,c). The final CDA loading in ZnCDA was 2.63 ± 0.08 wt%. The immunostimulatory activity of ZnCDA was validated using THP1 STING reporter cells (Supplementary Fig. 1c). In vivo studies demonstrated a dose-dependent anti-tumour effect of ZnCDA and transient reversible weight loss (Supplementary Fig. 1d,e). Based on these results, we selected a single dose of 10 μg CDA for further investigations. Moreover, measurements of aspartate transaminase (AST) and alanine transaminase (ALT) did not indicate systemic toxicity at a dose of 10 μg (Fig. 1d).

ZnCDA effectively suppressed tumour growth in a subcutaneous MC38 adenocarcinoma model (Fig. 1e) and a MC38 liver metastasis model (Fig. 1f–h). Most strikingly, all mice (5/5) bearing MC38 subcutaneous tumours and 5/7 of mice with MC38 liver metastases were tumour-free post ZnCDA treatment. Benchmark experiments showed that a single dose of ZnCDA was more potent than other non-CDN or non-formulated CDN STING agonists, including DMXAA, Diamidobenzimidazole (DiABZI) and 2′3′-cGAM(PS)$_2$ (R_p/S_p), even when others used at higher doses were demonstrated to be effective in experimental animals[15,20] (Supplementary Fig. 2a,b). In addition, ZnCDA exhibited superior tumour control in mice bearing B16F10 melanoma tumours (Fig. 1i) and prolonged survival in a BL3750 B-cell lymphoma model (Fig. 1j). A single dose of ZnCDA also induced anti-tumour effects in a Lewis lung carcinoma (LLC) model, which is refractory to STING agonist[21] (Supplementary Fig. 2c,d), and three doses of ZnCDA prevented tumour progression in transgenic adenocarcinoma of the mouse prostate (TRAMP) model (Supplementary Fig. 2e,f). Taken together, these results demonstrate ZnCDA can be administered systemically with potent anti-tumour activity in an array of primary and metastatic tumour models.

Liposomes are the most clinically used NP formulation with multiple Food and Drug Administration-approved formulations for cancer treatment[22]. To examine the improved performance of ZnCDA, we used a CDA-encapsulating liposome formulation (LipoCDA) as control (Supplementary Fig. 3a,b). ZnCDA greatly reduced CDA degradation in serum compared with LipoCDA, suggesting a better performance of the NCP compared with current standard formulations (Fig. 1k). ZnCDA also extended CDA circulation half-life in vivo (Fig. 1l and Supplementary Fig. 3c). Although LipoCDA extended the half-life of CDA from 0.21 to 3.30 hours, the half-life of CDA in ZnCDA was 12.63 hours (Fig. 1l). The increase in half-life led to a significantly greater reduction in tumour growth (Fig. 1m). Thus, the NCP platform protects CDA and provides pharmacokinetic advantages over conventional NP formulations, leading to an outstanding anti-tumour response.

ZnCDA disrupts tumour vasculature to promote tumour targeting

The enhanced permeability and retention (EPR) effect contributes to the passive tumour accumulation of NPs with diameters of 50–200 nm due to defective endothelial cell (EC) function, vascular leakiness and impaired lymphatic drainage[18,23]. To examine the biodistribution and tumour accumulation of ZnCDA, we loaded the NCPs with platinum only and platinum plus CDA, resulting in ZnP-Pt and ZnCDA-Pt, which could be traced by inductively coupled plasma mass spectrometry (ICP-MS). The half-life of ZnP-Pt (17.44 h) and ZnCDA-Pt (19.95 h) were similar (Fig. 2a). Interestingly, ZnCDA-Pt was more enriched in the tumour than ZnP-Pt (Fig. 2b), despite there being no accumulation differences in the liver or kidney (Supplementary Fig. 4). ZnCDA elicited similar anti-tumour effects on tumours with or without STING expression (Fig. 2c). In contrast, ZnCDA was ineffective in STING-deficient (*Tmem173*$^{-/-}$) mice (Fig. 2d), suggesting that the anti-tumour effect is dependent on host STING activation and not tumour STING activation. Early observations of increased tumour perfusion upon ZnCDA administration led us to hypothesize that host STING activation may contribute to changes in tumour vasculature, in turn amplifying the EPR effect and the accumulation of ZnCDA in tumours (Supplementary Fig. 5a). Haematoxylin and eosin (H&E) and CD31 immunohistochemistry (IHC) staining showed that ZnCDA-treated MC38 tumours had a 57.45% reduction in vessel density (Fig. 2e,f). Tumour vessel density was similarly decreased by 46.31% in B16F10 tumours (Supplementary Fig. 5b,c). Flow cytometry staining for CD31 and podoplanin (PDPN) confirmed that ZnCDA induced a significant decrease in tumour ECs ($CD45^-CD31^+PDPN^-$) (Supplementary Fig. 5d,e). Notably, ZnCDA did not affect vascular structures in the liver (Supplementary Fig. 5f,g), which is consistent with the similar uptake of Pt from ZnCDA-Pt and ZnP-Pt in the liver (Supplementary Fig. 4b). Moreover, there was no further accumulation of ZnCDA-Pt or tumour vasculature damage in *Tmem173*$^{-/-}$ mice (Fig. 2e,f), indicating that the targeted enrichment of ZnCDA is also host STING-dependent. To determine whether STING activation in the stromal or haematopoietic compartment contributes to the

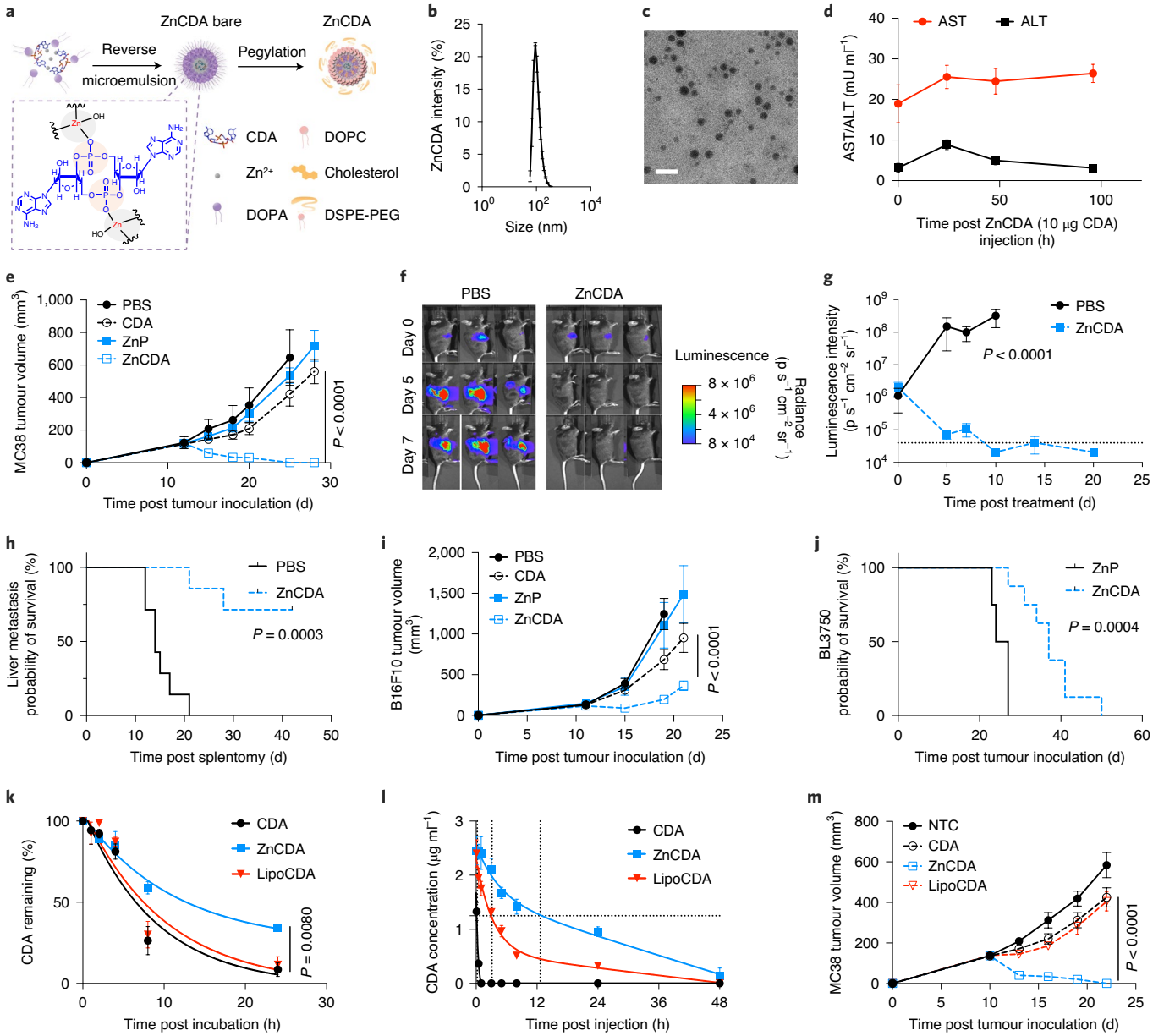

Fig. 1 | Systemic administration of ZnCDA suppresses primary and metastatic tumour growth in mice. a, Preparation and characterization of ZnCDA. **b**,**c**, *Z*-average size distribution (**b**) and transmission electron microscopy image (**c**) of ZnCDA. Scale bar, 100 nm. **d**, Analysis of ASL and ALT at different time points post ZnCDA treatment ($n = 9$ per group). **e**, Anti-tumour effects of free CDA, ZnCDA and ZnP on MC38 tumours in WT mice ($n = 5$ per group). PBS, phosphate-buffered saline. **f**, MC38-OVA-luciferase luminescence intensity of mouse livers after treatment with a control (PBS) and ZnCDA (three representative mice per group are shown). **g**, Luminescence intensity of MC38-OVA-luciferase liver metastasis at different time points post PBS or ZnCDA treatment ($n = 4$ per group). The horizontal dotted line represents the baseline luminescence intensity level for non-tumour-bearing mice. **h**, Survival curves of mice with liver metastasis post PBS or ZnCDA treatment, pooled from two independent experiments ($n = 7$ per group). **i**, Anti-tumour effects of free CDA, ZnCDA and ZnP on B16F10 tumours in WT mice ($n = 5$ per group). **j**, Survival curves showing the anti-tumour effect of ZnCDA and ZnP on BL3750 tumours in WT mice, pooled from two independent experiments ($n = 7$ per group). **k**, CDA degradation in serum, detected by liquid chromatography–mass spectrometry (LC–MS). The curves were plotted by a one-phase exponential decay fit ($n = 3$ per group). **l**, Pharmacokinetics of free CDA, LipoCDA and ZnCDA. The curves were plotted by a two-phase exponential decay fit ($n = 3$ per group). The horizontal and vertical dotted lines indicate the half-time. **m**, Anti-tumour effects of free CDA, LipoCDA and ZnCDA on MC38 tumours in WT mice ($n = 5$ per group). NTC, non-treated control. Data are represented as mean ± s.e.m. Two-way analysis of variance (ANOVA) tests were used to analyse the tumour growth curves. The log-rank (Mantel–Cox) test was used for the survival curves. One representative experiment out of two (**d**,**f**,**h**,**i**,**k**–**m**) or three (**b**,**c**,**e**,**g**,**k**) is shown.

targeted enrichment of ZnCDA, we generated wild-type (WT)→STING bone marrow chimeric mice, in which the radio-resistant stromal cells, including but not limited to ECs, lack STING expression. In contrast, in STING→WT mice, the haematopoietic cells lack STING expression. ZnCDA-treated tumours had a 22.79% reduction in vessel density in WT→STING mice (Supplementary Fig. 5h,i), and a 55.51% reduction in vessel density in STING→WT mice (Supplementary Fig. 5j,k). These results suggest that STING activation in radio-resistant cells is more important for the targeted enrichment of ZnCDA.

ECs are closely related to the entry of NPs into solid tumours, and intratumoural STING activation induces temporal changes in tumour vasculatures[24,25]. ZnCDA reduced tumour vessel density by 21.33% (Fig. 2h,i), and there was no targeted enrichment of ZnCDA in the EC-specific STING conditional knockout (*Tek*$^{\Delta STING}$) mice (Fig. 2j).

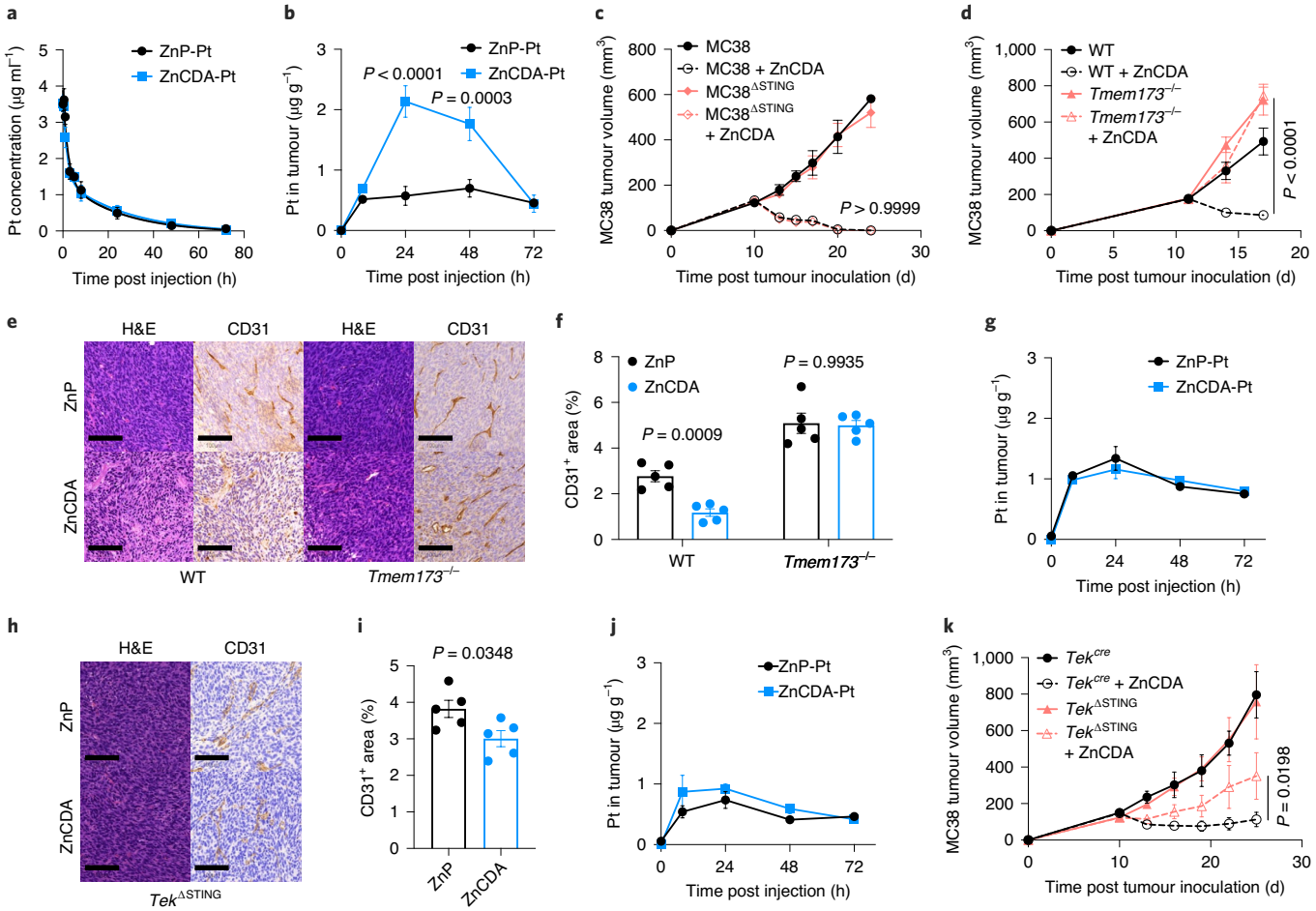

Fig. 2 | ZnCDA disrupts the tumour vasculature to enhance its deposition in tumours. a, Comparison of the pharmacokinetics of ZnCDA-Pt and ZnP-Pt. The curves were plotted according to a two-phase exponential decay fit ($n = 5$ per group). **b**, Kinetics of the tumour distribution of ZnCDA-Pt and ZnP-Pt in WT mice (μg Pt per g tumour, $n = 3$ per group). **c**, Anti-tumour effects of ZnCDA on MC38 and MC38$^{\Delta STING}$ tumours in WT mice ($n = 5$ per group). **d**, Anti-tumour effects of ZnCDA on MC38 tumours in WT or *Tmem173*$^{-/-}$ mice ($n = 5$ per group). **e**, H&E and CD31 IHC staining of tumours from WT or *Tmem173*$^{-/-}$ mice 24 hours post ZnCDA or ZnP treatment. Scale bars, 100 μm. **f**, Statistical summary of the CD31$^+$ area in the tumours shown in **e** ($n = 5$ per group, each dot represents an analyzed tumor section). **g**, Time-dependent tumour distributions of ZnCDA-Pt and ZnP-Pt in *Tmem173*$^{-/-}$ mice (μg Pt per g tumour, $n = 3$ per group). **h**, H&E and CD31 IHC staining of tumours from WT or *Tek*$^{\Delta STING}$ mice 24 hours post ZnCDA or ZnP treatment. Scale bars, 100 μm. **i**, Statistical summary of the CD31$^+$ area in the tumours shown in **h** ($n = 5$ per group, each dot represents an analyzed tumor section). **j**, Kinetics of the tumour distribution of ZnCDA-Pt and ZnP-Pt in *Tek*$^{\Delta STING}$ mice (μg Pt per g tumour, $n = 4$ per group). **k**, Anti-tumour effects of ZnCDA on MC38 tumours in *Tek*^{cre} and *Tek*$^{\Delta STING}$ mice ($n = 5$ per group). Data are presented as mean ± s.e.m. Two-way ANOVA tests were used to analyse the curve data. Unpaired *t*-tests were used to compare two groups. One representative experiment out of two (**a**,**c**,**e**–**i**) or three (**b**,**d**) experiments is shown.

Consequently, the anti-tumour effect of ZnCDA in *Tek*$^{\Delta STING}$ mice was partly abrogated (Fig. 2k). These findings indicate that EC STING activation is necessary for the tumour-targeted enrichment of ZnCDA. Interestingly, the anti-tumour effect of ZnCDA was impaired in WT→STING mice, but abrogated in STING→WT mice (Supplementary Fig. 5l,m), suggesting that STING activation in the haematopoietic compartment is a major contributor to the anti-tumour activity of ZnCDA. Taken together, ZnCDA enhances its own tumour accumulation and penetration by disrupting tumour vasculature. Although our results suggest that haematopoietic STING activation is critical for the anti-tumour activity of ZnCDA, we cannot rule out that an anti-angiogenetic effect of ZnCDA may contribute to the anti-tumour activity.

ZnCDA optimizes the antigen presentation capacity of TAMs

Cytokines and chemokines released from innate immune cells after STING activation protect the host from infections and promote an anti-tumour immune response[26]. Among these cytokines, IFN-I is recognized as an important driver of anti-tumour immunity[5,27]. As shown in Supplementary Fig. 6a–e, 24 hours after ZnCDA treatment there were significantly increased systemic levels of IFN-β, tumour-necrosis factor-α (TNF-α), IFN-γ, interleukin-6 (IL-6) and the myeloid recruiting chemokine CCL-2, no upregulation of which was observed in *Tmem173*$^{-/-}$ mice (Supplementary Fig. 6a–e).

To determine whether IFN-I signalling is critical for the anti-tumour activity of ZnCDA, we blocked the IFN-I pathway using a blocking antibody or IFN-I receptor knockout (*Ifnar1*$^{-/-}$) mice. Interestingly, ZnCDA retained its anti-tumour activity in mice treated with anti-IFNAR1 (Fig. 3a) and in *Ifnar1*$^{-/-}$ mice (Fig. 3b), suggesting that ZnCDA could suppress tumour growth in the absence of host IFN-I signalling. As STING activation leads to the induction of IFN-I through the phosphorylation of IRF3, we also investigated the anti-tumour effect of ZnCDA in *Irf3*$^{-/-}$ mice, which again responded to ZnCDA (Supplementary Fig. 6f). IFN-I can also suppress tumour growth through their intrinsic functions in tumour cells[28]. In both WT and *Ifnar1*$^{-/-}$ mice, the knockout of IFNAR1 in MC38 tumour cells (MC38$^{\Delta IFNAR1}$) had no effect on the anti-tumour activity of ZnCDA (Fig. 3c,d). In contrast, ZnCDA was ineffective in *Ifng*$^{-/-}$ mice (Fig. 3e) but was not affected by anti-TNF-α, anti-IL-6R blockade

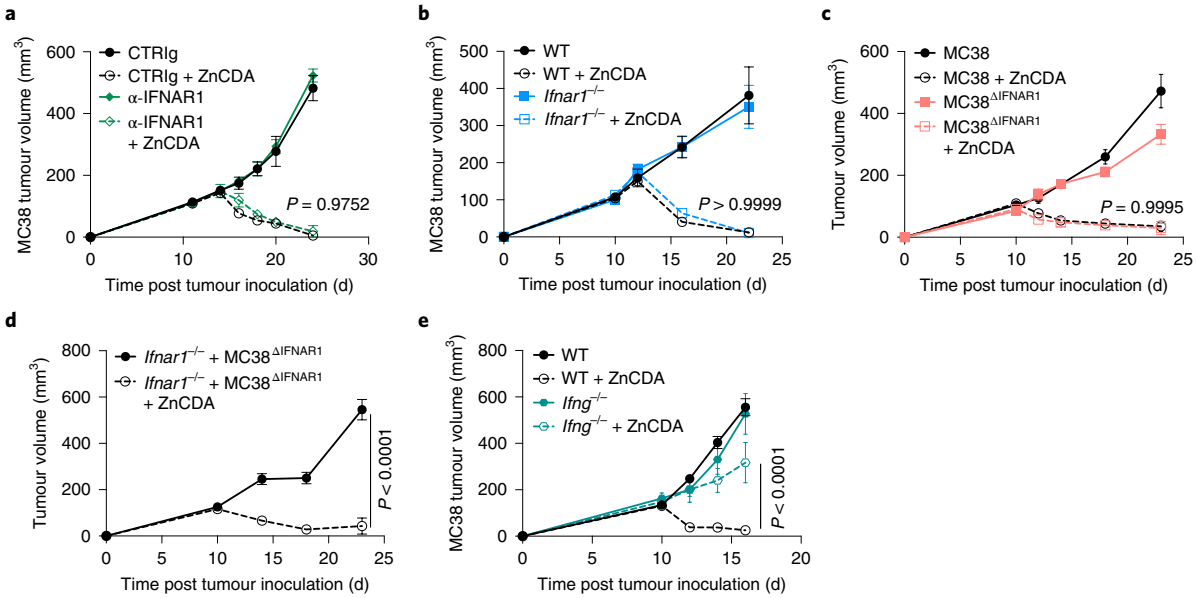

Fig. 3 | IFN-γ instead of IFN-I is necessary for ZnCDA-induced tumour suppression. a, Anti-tumour effects of ZnCDA on MC38 tumours in WT mice treated with anti-IFNAR1 (α-IFNAR1) blockade or control antibody (CTRIg) ($n = 5$ per group). **b**, Anti-tumour effects of ZnCDA on MC38 tumours in WT and *Ifnar1*$^{-/-}$ mice ($n = 5$ per group). **c**, Anti-tumour effects of ZnCDA on MC38 and MC38$^{\Delta IFNAR1}$ tumours in WT mice ($n = 5$ per group). **d**, Anti-tumour effects of ZnCDA on MC38$^{\Delta IFNAR1}$ tumours in *Ifnar1*$^{-/-}$ mice ($n = 5$ per group). **e**, Anti-tumour effects of ZnCDA on MC38 tumours in WT and *Ifng*$^{-/-}$ mice ($n = 5$ per group). Data are represented as mean ± s.e.m. Two-way ANOVA tests were used to analyse the curve data. One representative experiment out of two (**d**,**e**) or three (**a**–**c**) experiments is shown.

or chemokine receptor CCR2 deficiency (Supplementary Fig. 6g–i). These findings suggest that IFN-γ, rather than IFN-I, is required for the therapeutic effect of ZnCDA.

IFN-γ is a cytokine primarily produced by immune cells, including innate-like lymphocyte populations such as natural killer (NK) cells, γδ T cells and type I innate lymphoid cells (ILC1s), as well as adaptive immune cells, such as T helper 1 (Th1) and CD8$^+$ cytotoxic T lymphocytes (CTLs)[29,30]. As shown in Supplementary Fig. 7, there were no infiltration changes in NK cells (CD45$^+$NK1.1$^+$CD3$^-$), γδ T cells (CD45$^+$TCRγδ$^+$CD3$^+$) or ILC1s (CD45$^+$CD127$^+$Lineage$^-$CD117$^-$ICOS$^-$) in the TME post ZnCDA treatment (Supplementary Fig. 7a–g). CD8$^+$ T cells increased while CD4$^+$ T cells were unaffected on day 7 after ZnCDA treatment (Supplementary Fig. 7h,i). ZnCDA also induced tumour-specific IFN-γ-secreting CD8$^+$ and CD4$^+$ T cells in an ovalbumin-expressing MC38 (MC38-OVA) model (Fig. 4a). Furthermore, the anti-tumour activity of ZnCDA was abrogated after the depletion of CD4$^+$ and CD8$^+$ T cells (Fig. 4b). Separately, CD8$^+$ T-cell depletion led to a more pronounced inhibition of anti-tumour activity (Fig. 4c,d), suggesting CD8$^+$ T cells play a critical role in ZnCDA activity.

We next sought to examine the role of tumour pre-existing and newly infiltrating T cells in response to ZnCDA. FTY720 is a structural analogue of sphingosine-1-phosphate, which inhibits the egress of T cells from lymph nodes into circulation and peripheral tissues[31]. Mice were treated with FTY720 either before tumour inoculation (preFTY720) or concurrently with ZnCDA treatment (postFTY720) to distinguish the role of pre-existing or infiltrating T cells. PreFTY720 impaired the effectiveness of ZnCDA (Fig. 4e), indicating that pre-existing T cells are important for ZnCDA activity. Tumours in mice treated with postFTY720 still responded to ZnCDA (Fig. 4f), demonstrating that pre-existing T cells are sufficient for anti-tumour effects in MC38 tumours. When intratumoural CD8$^+$ T cells were depleted during postFTY720 and ZnCDA treatment, the therapeutic effect of ZnCDA was abrogated (Fig. 4f).

We previously reported a Panc02-SIY (with SIYRYYGL peptide expression) tumour model to mimic the poorly inflamed pancreatic cancer phenotype through fragment transplantation[32]. The pre-infiltration of CD8$^+$ T cells in MC38 tumours is approximately 100-fold greater than that in Panc02-SIY tumours (Supplementary Fig. 7j). ZnCDA partially suppressed the growth of Panc02-SIY tumours, and its effect was abrogated with postFTY720 treatment (Supplementary Fig. 7k). This indicates that while pre-existing T cells are important, infiltrating T cells can contribute to the anti-tumour response.

Murine and human tumours harbour stem-like TCF1$^+$PD-1$^+$CD8$^+$ T cells with the capacity to expand, regenerate and differentiate into effector T cells in response to immunotherapy[33]. Similarly, we found an increase in intratumoural TCF1$^+$PD-1$^+$CD8$^+$ and TCF1$^-$PD-1$^+$CD8$^+$ T cells after treatment with ZnCDA and postFTY720 (Fig. 4g–i). Most of the TCF1$^+$PD-1$^+$CD8$^+$ T cells were Ly108$^+$CXCR5$^+$CD127$^+$Tim3$^-$, approximately 50% of which were highly proliferative (Supplementary Fig. 7l), suggesting that ZnCDA promotes a sustained production of differentiated effector cells from pre-infiltrated TCF1$^+$PD-1$^+$CD8$^+$ T cells in the TME. These results demonstrate that, in T-cell-inflamed tumours, pre-existing CD8$^+$ T cells are sufficient for the anti-tumour activity of ZnCDA. The ability of ZnCDA to activate pre-infiltrated T cells in the TME could be used to rejuvenate anti-tumour immunity.

To investigate the cellular target of ZnCDA, the NCPs were tagged with the tracer dye rhodamine B (Rho), resulting in ZnCDA-Rho and ZnP-Rho. Six hours after injection, we observed a significant Rho signal in both intratumoural CD45$^+$ cells (Supplementary Fig. 8a,b) and tumour cells (Supplementary Fig. 8c,d). Both ZnP-Rho and ZnCDA-Rho preferentially targeted TAMs (CD45$^+$CD11b$^+$F4/80$^+$), but not T cells (CD45$^+$CD4$^+$ or CD45$^+$CD8$^+$) in the TME (Supplementary Fig. 8e). The cellular target was confirmed using Zr-labelled ZnP. At 24 hours post injection, tumour-associated cells were isolated and the amount of Zr was quantified by ICP-MS. As is shown in Supplementary Fig. 8f, CD11b$^+$ cells contained the highest concentration of Zr, suggesting that the NCPs preferentially target the CD11b$^+$ population in the TME.

To further study the effect of ZnCDA on TAMs, bulk RNA sequencing (RNA-seq) was performed on CD45$^+$CD11b$^+$F4/80$^+$Rho$^+$ TAMs collected 6 hours after ZnP-Rho or ZnCDA-Rho injection. Gene set enrichment analysis (GSEA) of ZnCDA-targeted TAMs showed the upregulation of transcripts related to immune activation as well as

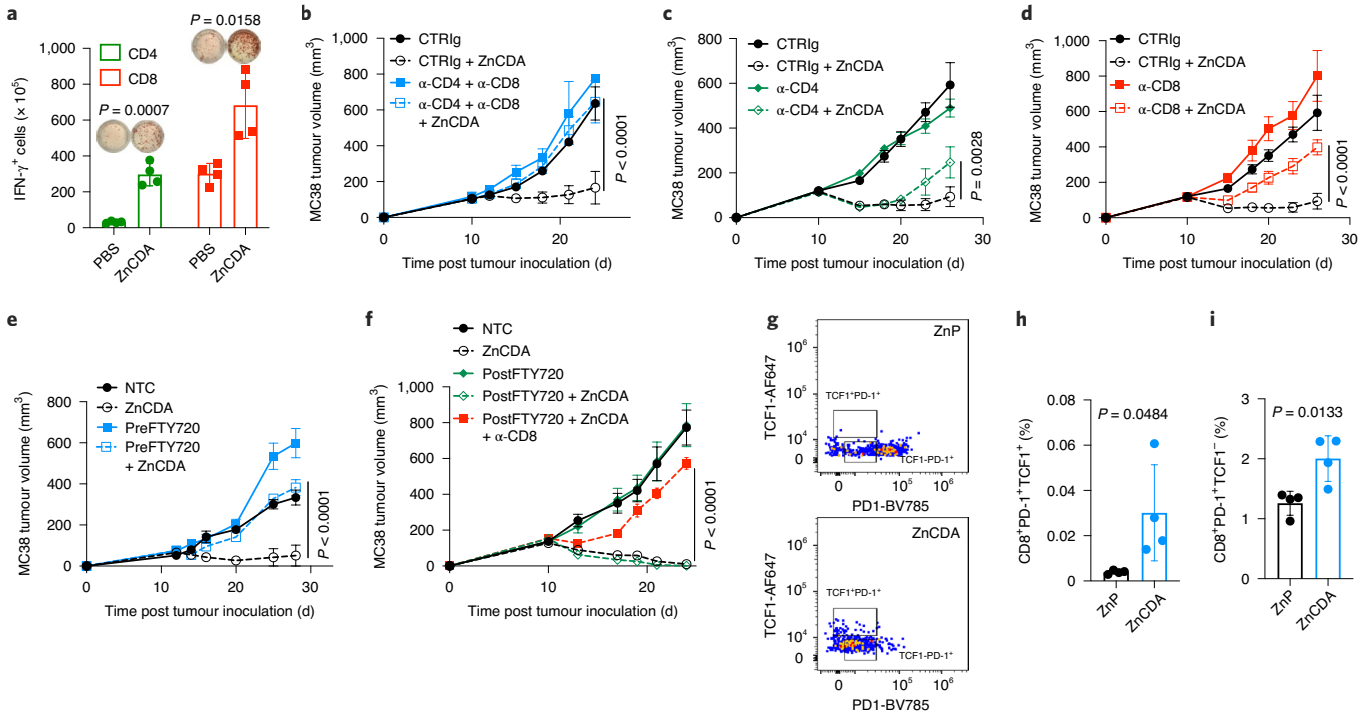

Fig. 4 | Tumour pre-existing T cells are sufficient and critical for the anti-tumour effect in T-cell-inflamed tumours. a, Intratumoural IFN-γ$^+$ T-cell responses in MC38-OVA tumours on day 7 post ZnCDA treatment ($n = 4$ per group, each dot represents one sample from one mouse). **b**, Anti-tumour effects of ZnCDA on MC38 tumours in WT mice with CD4$^+$ and CD8$^+$ T-cell depletion ($n = 5$ per group). **c**, Anti-tumour effects of ZnCDA on MC38 tumours in WT mice with CD4$^+$ T-cell depletion ($n = 5$ per group). **d**, Anti-tumour effects of ZnCDA on MC38 tumours in WT mice with CD8$^+$ T-cell depletion ($n = 5$ per group). **e**, Anti-tumour effects of ZnCDA on MC38 tumours in WT mice with preFTY720 treatment ($n = 5$ per group). **f**, Anti-tumour effects of ZnCDA on MC38 tumours in WT mice with postFTY720 treatment and pre-existing CD8$^+$ T-cell depletion ($n = 5$ per group). **g**–**i**, CD8$^+$ cells were gated according to the strategy shown in Supplementary Fig. 7a,h. Percentages of pre-existing CD8$^+$PD-1$^+$TCF1$^+$ and CD8$^+$PD-1$^+$TCF1$^-$ T cells gated from CD45$^+$ cells in tumours post ZnCDA and postFTY720 treatment ($n = 4$ per group). Representative dot plots (**g**) and statistical results for CD45$^+$CD8$^+$PD-1$^+$TCF1$^+$ (**h**) and CD45$^+$CD8$^+$PD-1$^+$TCF1$^-$ (**i**) cells; each dot represents one sample from one mouse. Data are represented as mean ± s.e.m. Two-way ANOVA tests were used to analyse the curve data. Unpaired *t*-tests were used to compare two groups. One representative experiment out of two is shown.

the stimulation of inflammatory cytokines and IFN-I signalling pathways (Fig. 5a,b). The antigen processing and presentation pathway was among the top upregulated KEGG (Kyoto Encyclopedia of Genes and Genomes) gene sets in ZnCDA-targeted TAMs (Fig. 5a,c), and M1 polarization was among the top upregulated Hallmark gene sets (Fig. 5b,d). Consistent with the GSEA, ZnCDA-targeted TAMs exhibited downregulation in lysosomal enzymatic processes and M2 polarization, but upregulation in antigen presentation and M1 polarization (Fig. 5e). Accumulating evidence suggests that STING agonism repolarizes M2 macrophages towards an M1-like subtype[34,35]. Given the upregulation in antigen presentation pathways, we hypothesized that the ZnCDA-targeted TAMs may play a pivotal role in the priming of intratumoural T cells, during which their polarization towards M1 could facilitate anti-tumour immunity.

In the TME, lysosomal degradation functions to process tumour-associated antigens, which are loaded onto major histocompatibility complex (MHC) molecules for recognition by T cells[36]. Compared with dendritic cells (DCs), macrophages typically contain higher levels of lysosomal proteases that rapidly degrade internalized proteins, thereby limiting their antigen presentation capacity[37]. However, ZnCDA downregulated the lysosomal enzyme-related genes in TAMs (Fig. 5e). Furthermore, ovalbumin (OVA) labelled with the pH-insensitive fluorescent dye Alexa Fluor 647 (OVA-AF647) was used to detect antigen uptake. DQ-OVA, a self-quenched conjugate of OVA showing bright-green fluorescence upon proteolytic degradation, was used to detect antigen degradation. Free CDA, ZnCDA and ZnP had no effect on antigen uptake in WT bone marrow-derived macrophages (BMDMs; Fig. 5f). In contrast, free CDA and ZnCDA, but not ZnP, attenuated antigen degradation in WT BMDMs (Fig. 5g). This effect was abolished in BMDMs derived from *Tmem173*$^{-/-}$ mice (Supplementary Fig. 8g,h) but remained in *Ifnar1*$^{-/-}$ BMDMs (Supplementary Fig. 8i). In addition, ZnCDA administration enhanced the T-cell priming ability of *Ifnar1*$^{-/-}$ BMDMs (Supplementary Fig. 8j), which is consistent with a recent report indicating that the STING-induced upregulation of antigen presentation pathways in BMDMs is independent of IFN-I[38]. These findings indicate that STING activation in macrophages retards antigen degradation, which in turn likely promotes antigen presentation to T cells in the TME.

When detected in vivo, CD45$^+$CD11b$^+$CD11c$^-$Ly6C$^-$MHCII$^+$ cells increased in the TME post ZnCDA administration (Supplementary Fig. 8k,l) and the expression of co-stimulatory factors (CD80 and CD86) and MHC class I (MHCI) in ZnCDA-targeted TAMs (CD45$^+$CD11b$^+$F4/80$^+$Rho$^+$) was upregulated (Fig. 5h and Supplementary Fig. 8m). NCP-targeted TAMs were isolated from OT-I-tagged MC38 (MC38-OT-I) tumours 3 days after treatment and co-cultured with OT-I T cells. ZnCDA-targeted TAMs primed more IFN-γ$^+$CD8$^+$ OT-I T cells, indicating their enhanced antigen presentation ability (Fig. 5i). To determine whether TAMs were critical for the anti-tumour activity of ZnCDA, macrophages were depleted in vivo by the blockade of colony-stimulating factor 1 receptor (CSF1R) signalling. Anti-CSF1R induced a significant reduction in the proportion of CD11b$^+$F4/80$^+$ TAMs (Supplementary Fig. 8n,q) and a modest, but not significant increase in neutrophils and cDC2 cells (Supplementary Fig. 8o–q) in the TME, and reversed the increase in CD45$^+$CD11b$^+$CD11c$^-$Ly6C$^-$MHCII$^+$ cells (Fig. 5j) and diminished the tumour antigen-specific CD8$^+$ T-cell response (Fig. 5k) following ZnCDA treatment. Consistent with these

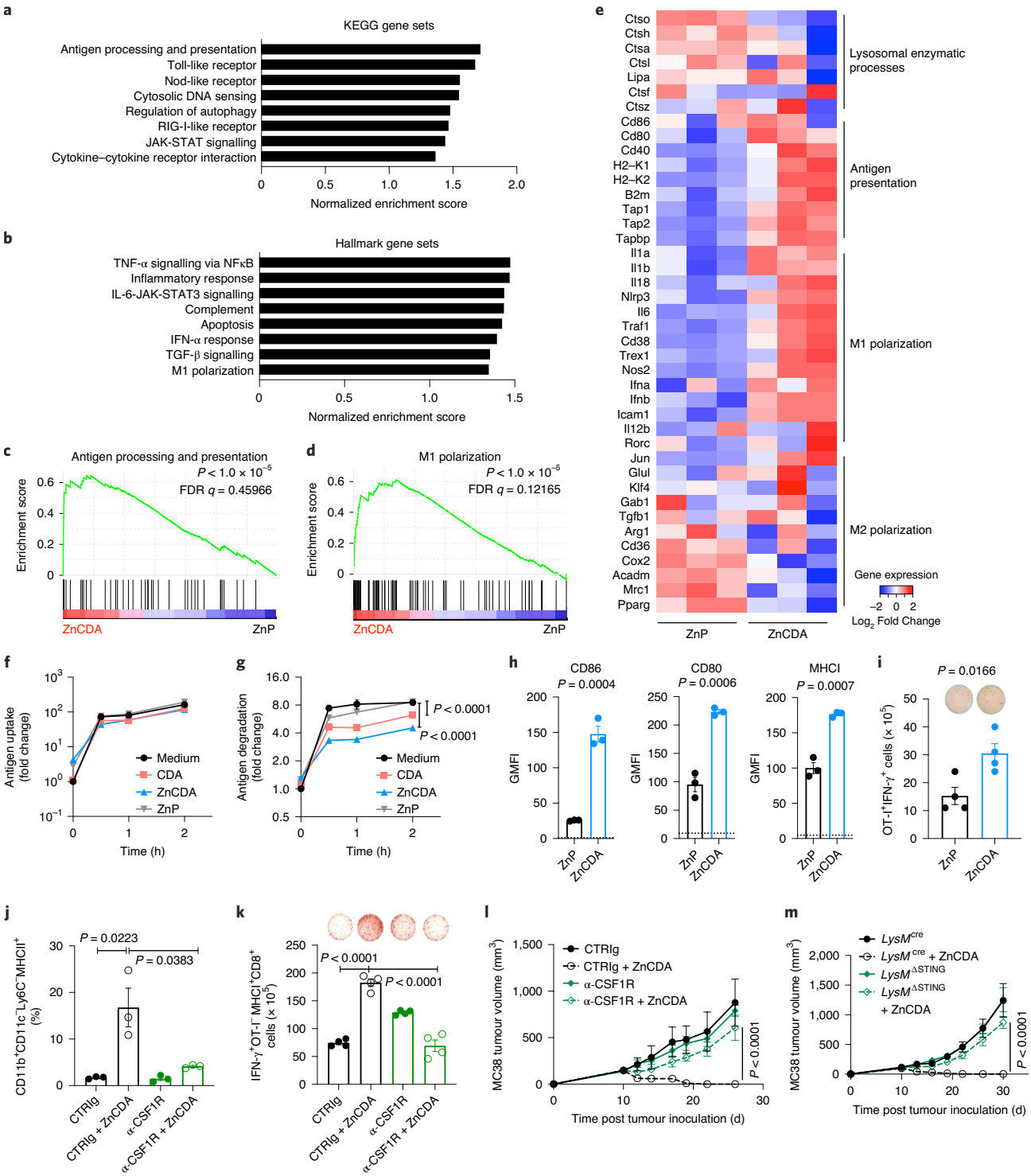

Fig. 5 | ZnCDA targets TAMs in the TME and modulates their antigen processing and presentation ability. a,**b**, Top eight enriched pathways among KEGG (**a**) and Hallmark (**b**) gene sets in ZnCDA-treated TAMs. **c**,**d**, Mountain plots of the antigen processing and presentation (**c**) and M1 polarization (**d**) pathways. FDR, false discovery rate. Nominal *P* values are shown. Stick plots at the bottom represent the position in the ranked list of genes. **e**, Heatmap comparing genes related to lysosomal enzymatic processes, antigen presentation, and M1 and M2 polarization post ZnP or ZnCDA treatment. **f**,**g**, OVA uptake (**f**) and degradation (**g**) in WT BMDMs post treatment with free CDA, ZnCDA or ZnP ($n = 3$ per group). **h**, Comparison of Geometric Mean Fluorescence Intensity of CD86, CD80 and MHCI expression in $CD45^+CD11b^+F4/80^+Rho^+$ cells post ZnP or ZnCDA treatment ($n = 3$ per group, each dot represents one sample from one mouse). **i**, T-cell priming ability of $CD45^+CD11b^+F4/80^+Rho^+$ cells post ZnP or ZnCDA treatment ($n = 4$ per group, each dot represents one sample from one mouse). **j**, Percentage of intratumoural $CD11b^+CD11c^-Ly6C^-MHCII^+$ cells gated from $CD45^+$ cells in anti-CSF1R-treated mice 24 hours post ZnCDA treatment ($n = 3$ per group, each dot represents one sample from one mouse). **k**, Intratumoural cytotoxic T-cell response in MC38-OT-I tumours post ZnCDA and anti-CSF1R treatment ($n = 4$ per group, each dot represents one sample from one mouse). **l**, Anti-tumour effects of ZnCDA on MC38 tumours in WT mice with anti-CSF1R (α-CSF1R) and control antibody (CTRIg) treatment ($n = 5$ per group). **m**, Anti-tumour effects of ZnCDA on MC38 tumours in $LysM^{cre}$ and $LysM^{\Delta STING}$ mice ($n = 5$ per group). Data are represented as mean ± s.e.m. Two-way ANOVA tests were used to analyse the curve data. Unpaired *t*-tests were used to compare two groups. One representative experiment out of two (**f**–**l**) or three (**m**) is shown.

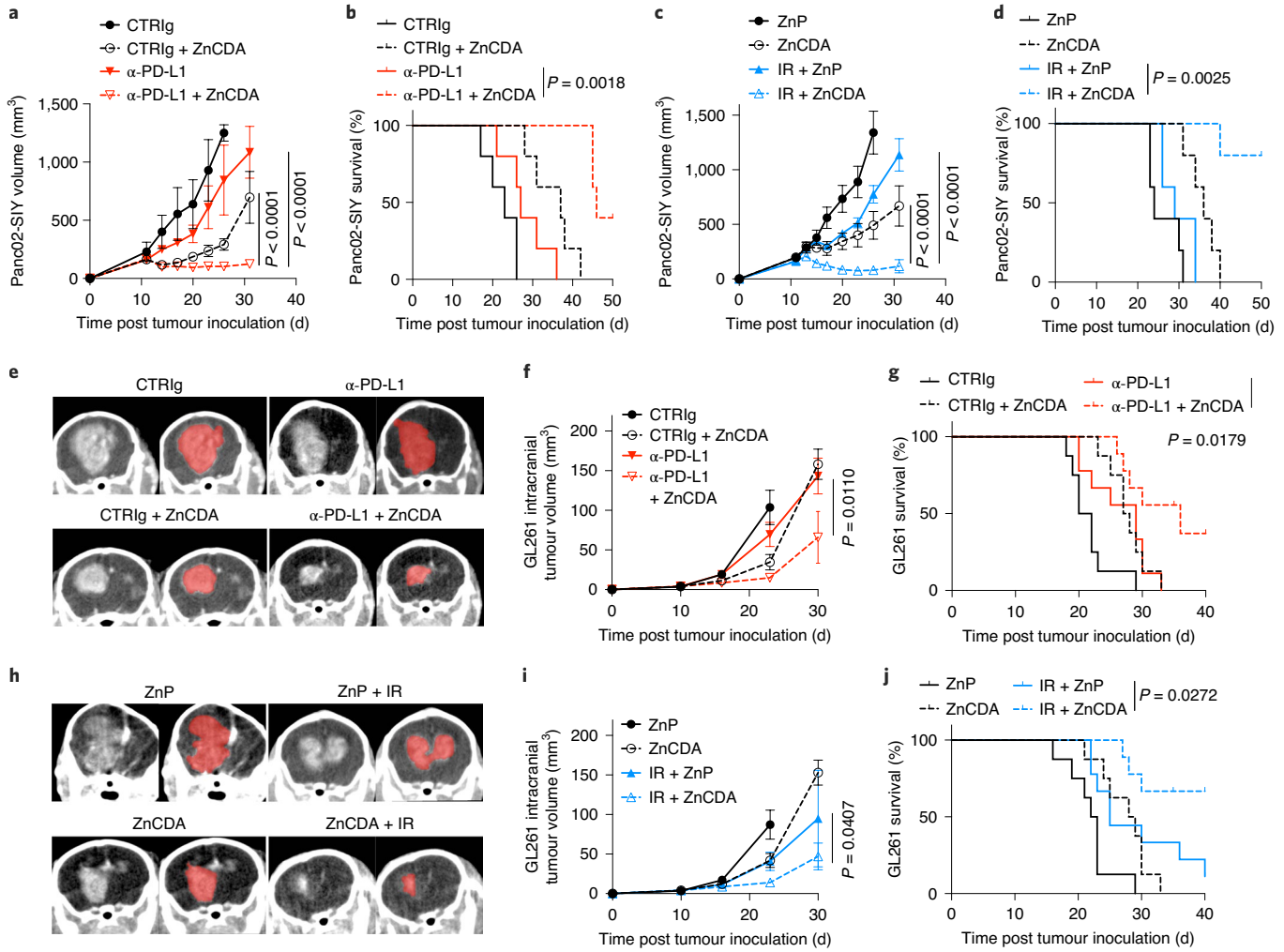

Fig. 6 | ZnCDA combines with ICB or IR to overcome treatment resistance. **a**, Anti-tumour effects of ZnCDA and anti-PD-L1 on Panc02-SIY tumours in WT mice ($n = 5$ per group). **b**, Survival curves showing the anti-tumour effects of ZnCDA and anti-PD-L1 on Panc02-SIY tumours in WT mice ($n = 5$ per group). **c**, Anti-tumour effects of ZnCDA and IR on Panc02-SIY tumours in WT mice ($n = 5$ per group). **d**, Survival curves showing the anti-tumour effects of ZnCDA and IR on Panc02-SIY tumours in WT mice ($n = 5$ per group). **e**, Micro-computed tomography (microCT) images of GL261 gliomas in mice with single and combined treatment of ZnCDA and anti-PD-L1 on day 20 post tumour inoculation. **f**, Anti-tumour effects of ZnCDA and anti-PD-L1 on GL261 gliomas in WT mice ($n = 10$ per group, pooled from two independent experiments). **g**, Survival curves showing the anti-tumour effects of ZnCDA and anti-PD-L1 on GL261 gliomas in WT mice ($n = 10$ per group, pooled from two independent experiments). **h**, MicroCT images of GL261 gliomas in mice with single or combined treatment of ZnP, ZnCDA and IR on day 20 post tumour inoculation. **i**, Anti-tumour effects of ZnCDA and IR on GL261 gliomas in WT mice ($n = 10$ per group, pooled from two independent experiments). **j**, Survival curves showing the anti-tumour effects of ZnCDA and IR on GL261 gliomas in WT mice ($n = 10$ per group, pooled from two independent experiments). Data are represented as mean ± s.e.m. Two-way ANOVA tests were used to analyse the tumour growth curve. The log-rank (Mantel–Cox) test was used for the survival curves. One representative experiment out of two is shown.

findings, anti-CSF1R abrogated the anti-tumour activity of ZnCDA (Fig. 5l). Similarly, we observed a diminished response in monocyte/macrophage-conditional STING knockout mice (*LysM*$^{\Delta STING}$; Fig. 5m). Taken together, these results demonstrate that ZnCDA preferentially targets TAMs and optimizes their tumour antigen presentation function through macrophage endogenous STING activation.

ZnCDA overcomes immunotherapy and radiotherapy resistance

Non-T-cell-inflamed (cold) tumours present a clinical challenge even in the era of immunotherapy, and many patients obtain limited benefit from monotherapy[39]. The Panc02-SIY model mimics non-inflamed pancreatic cancer and fails to respond to immune checkpoint blockade (ICB) or ionizing radiation (IR) alone[32]. Importantly, CD8$^+$ T cells and tumour-specific CD8$^+$SIY-pentamer$^+$ T cells increased in the TME post ZnCDA treatment (Supplementary Fig. 9a,b). Excitingly, ZnCDA overcame anti-PD-L1 resistance to control Panc02-SIY tumour growth and extended mouse survival (Fig. 6a,b). When co-treated with IR and ZnCDA, 2/5 of tumour-bearing mice were tumour-free 40 days post treatment (Fig. 6c,d).

Glioma is difficult to treat due to intrinsic resistance and/or poor blood–brain barrier penetration; standard treatment is surgery followed by radiotherapy and chemotherapy[40]. Although the clinical efficacy of PD-1/PD-L1 blockade in glioma is still controversial, more and more studies are exploring combination strategies[41]. An orthotopic glioma model was established by intracranial injection of GL261 cells. Following intravenous administration, ZnCDA was able to pass the blood–brain barrier (Supplementary Fig. 4f). As expected, T cells are sparse in the GL261 model, but increased upon ZnCDA administration (Supplementary Fig. 9c,d). Again, ZnCDA reversed the resistance of glioma to anti-PD-L1 treatment, resulting in prolonged survival (Fig. 6e–g). Moreover, ZnCDA potentiated the IR-induced anti-tumour

effect in the glioma model (Fig. 6h–j). Thence, we propose that the combination of ZnCDA with ICB or IR could be considered as a clinical strategy for unresponsive cancers.

Conclusions

Applications of nanomaterials have garnered attention in cancer therapy due to their ability to enhance the delivery of chemotherapeutics, genes and immunostimulants. We have developed a nanoformulated tumour-targeting STING activator, ZnCDA, based on the NCP platform, that has advantages over conventional NPs for small hydrophilic molecule delivery. Unexpectedly, STING activation in tumour ECs resulted in rapid vasculature disruption, which further enhanced the tumour accumulation of ZnCDA. It is possible that EC STING activation can be exploited to increase tumour-targeted drug delivery.

Studies following the intratumoural administration of STING agonists suggested that IFN-I is indispensable for STING activation-mediated anti-tumour effects. Our study indicates that different formulation or delivery strategies may suppress tumour growth through alternative pathways, presenting a major therapeutic advantage. We have found that ZnCDA preferentially targets and modulates the antigen processing and presentation of TAMs, which further promotes the anti-tumour T-cell response. The blockade of CSF1R signalling reduces TAMs and eliminates the anti-tumour ability of ZnCDA (Supplementary Fig. 10). Taken together, ZnCDA enhances its own tumour targeting, reinvigorates TAMs to promote anti-tumour T-cell immunity and overcomes a 'cold' phenotype. Moreover, the combination of ZnCDA and ICB or IR provides a proof-of-concept therapeutic strategy for overcoming resistance to intractable human cancers.

Online content

Any methods, additional references, Nature Research reporting summaries, source data, extended data, supplementary information, acknowledgements, peer review information; details of author contributions and competing interests; and statements of data and code availability are available at https://doi.org/10.1038/s41565-022-01225-x.

References

1. Sun, L., Wu, J., Du, F., Chen, X. & Chen, Z. J. Cyclic GMP-AMP synthase is a cytosolic DNA sensor that activates the type I interferon pathway. *Science* **339**, 786–791 (2013).
2. Wu, J. et al. Cyclic GMP-AMP is an endogenous second messenger in innate immune signaling by cytosolic DNA. *Science* **339**, 826–830 (2013).
3. Ishikawa, H., Ma, Z. & Barber, G. N. STING regulates intracellular DNA-mediated, type I interferon-dependent innate immunity. *Nature* **461**, 788–792 (2009).
4. Chen, Q., Sun, L. & Chen, Z. J. Regulation and function of the cGAS–STING pathway of cytosolic DNA sensing. *Nat. Immunol.* **17**, 1142–1149 (2016).
5. Deng, L. et al. STING-dependent cytosolic DNA sensing promotes radiation-induced type I interferon-dependent antitumor immunity in immunogenic tumors. *Immunity* **41**, 843–852 (2014).
6. Pantelidou, C. et al. PARP inhibitor efficacy depends on $CD8^+$ T-cell recruitment via intratumoral sting pathway activation in BRCA-deficient models of triple-negative breast cancer. *Cancer Discov.* **9**, 722–737 (2019).
7. Wang, Z. et al. cGAS/STING axis mediates a topoisomerase II inhibitor-induced tumor immunogenicity. *J. Clin. Invest.* **129**, 4850–4862 (2019).
8. Parkes, E. E. et al. Activation of STING-dependent innate immune signaling by S-phase-specific DNA damage in breast cancer. *J. Natl Cancer Inst.* **109**, djw199 (2017).
9. Mender, I. et al. Telomere stress potentiates STING-dependent anti-tumor immunity. *Cancer Cell* **38**, 400–411.e6 (2020).
10. Lara, P. N. et al. Randomized phase III placebo-controlled trial of carboplatin and paclitaxel with or without the vascular disrupting agent vadimezan (ASA404) in advanced non-small-cell lung cancer. *J. Clin. Oncol.* **29**, 2965–2971 (2011).
11. Gao, P. et al. Binding-pocket and lid-region substitutions render human STING sensitive to the species-specific drug DMXAA. *Cell Rep.* **8**, 1668–1676 (2014).
12. Ding, C., Song, Z., Shen, A., Chen, T. & Zhang, A. Small molecules targeting the innate immune cGAS–STING–TBK1 signaling pathway. *Acta Pharm. Sin. B* **10**, 2272–2298 (2020).
13. Meric-Bernstam, F. et al. Phase Ib study of MIW815 (ADU-S100) in combination with spartalizumab (PDR001) in patients (pts) with advanced/metastatic solid tumors or lymphomas. *J. Clin. Oncol.* **37**, 2507–2507 (2019).
14. Pan, B. S. et al. An orally available non-nucleotide STING agonist with antitumor activity. *Science* https://doi.org/10.1126/science.aba6098 (2020).
15. Sun, X. et al. Amplifying STING activation by cyclic dinucleotide–manganese particles for local and systemic cancer metalloimmunotherapy. *Nat. Nanotechnol.* **16**, 1260–1270 (2021).
16. Yao, Y. et al. Nanoparticle-based drug delivery in cancer therapy and its role in overcoming drug resistance. *Front. Mol. Biosci.* **7**, 193 (2020).
17. Irvine, D. J. & Dane, E. L. Enhancing cancer immunotherapy with nanomedicine. *Nat. Rev. Immunol.* **20**, 321–334 (2020).
18. Sykes, E. A., Chen, J., Zheng, G. & Chan, W. C. W. Investigating the impact of nanoparticle size on active and passive tumor targeting efficiency. *ACS Nano* **8**, 5696–5706 (2014).
19. Duan, X. et al. Immunostimulatory nanomedicines synergize with checkpoint blockade immunotherapy to eradicate colorectal tumors. *Nat. Commun.* **10**, 1899 (2019).
20. Corrales, L. et al. Direct activation of STING in the tumor microenvironment leads to potent and systemic tumor regression and immunity. *Cell Rep.* **11**, 1018–1030 (2015).
21. Lemos, H. et al. Overcoming resistance to STING agonist therapy to incite durable protective antitumor immunity. *J. Immunother. Cancer* **8**, e001182 (2020).
22. Bulbake, U., Doppalapudi, S., Kommineni, N. & Khan, W. Liposomal formulations in clinical use: an updated review. *Pharmaceutics* **9**, 12 (2017).
23. Fang, J., Nakamura, H. & Maeda, H. The EPR effect: unique features of tumor blood vessels for drug delivery, factors involved, and limitations and augmentation of the effect. *Adv. Drug Deliv. Rev.* **63**, 136–151 (2011).
24. Kingston, B. R. et al. Specific endothelial cells govern nanoparticle entry into solid tumors. *ACS Nano* **15**, 14080–14094 (2021).
25. Yang, H. et al. STING activation reprograms tumor vasculatures and synergizes with VEGFR2 blockade. *J. Clin. Invest.* **129**, 4350–4364 (2019).
26. Barber, G. N. STING: infection, inflammation and cancer. *Nat. Rev. Immunol.* **15**, 760–770 (2015).
27. Xia, T., Konno, H., Ahn, J. & Barber, G. N. Deregulation of STING signaling in colorectal carcinoma constrains DNA damage responses and correlates with tumorigenesis. *Cell Rep.* **14**, 282–297 (2016).
28. Sangfelt, O. & Strander, H. Apoptosis and cell growth inhibition as antitumor effector functions of interferons. *Med. Oncol.* **18**, 3–14 (2001).
29. Ivashkiv, L. B. IFNγ: signalling, epigenetics and roles in immunity, metabolism, disease and cancer immunotherapy. *Nat. Rev. Immunol.* **18**, 545–558 (2018).
30. Gao, Y. et al. γδ T cells provide an early source of interferon γ in tumor immunity. *J. Exp. Med.* **198**, 433–442 (2003).
31. Adachi, K. & Chiba, K. FTY720 story. Its discovery and the following accelerated development of sphingosine 1-phosphate

receptor agonists as immunomodulators based on reverse pharmacology. *Perspect. Med. Chem.* **1**, 11–23 (2007).
32. Zheng, W. et al. Combination of radiotherapy and vaccination overcome checkpoint blockade resistance. *Oncotarget* **7**, 43039–43051 (2016).
33. Siddiqui, I. et al. Intratumoral Tcf1^{+}PD-1^{+}CD8^{+} T cells with stem-like properties promote tumor control in response to vaccination and checkpoint blockade immunotherapy. *Immunity* **50**, 195–211. e10 (2019).
34. Cheng, N. et al. A nanoparticle-incorporated STING activator enhances antitumor immunity in PD-L1-insensitive models of triple-negative breast cancer. *JCI insight* https://doi.org/10.1172/jci.insight.120638 (2018).
35. Ohkuri, T., Kosaka, A., Nagato, T. & Kobayashi, H. Effects of STING stimulation on macrophages: STING agonists polarize into 'classically' or 'alternatively' activated macrophages? *Hum. Vaccin. Immunother.* **14**, 285–287 (2018).
36. You, L. et al. The crosstalk between autophagic and endo-/exosomal pathways in antigen processing for MHC presentation in anticancer T cell immune responses. *J. Hematol. Oncol.* **10**, 165 (2017).
37. Delamarre, L., Pack, M., Chang, H., Mellman, I. & Trombetta, E. S. Differential lysosomal proteolysis in antigen-presenting cells determines antigen fate. *Science* **307**, 1630–1634 (2005).
38. Wu, J., Dobbs, N., Yang, K. & Yan, N. Interferon-independent activities of mammalian STING mediate antiviral response and tumor immune evasion. *Immunity* **53**, 115–126.e5 (2020).
39. Smyth, M. J., Ngiow, S. F., Ribas, A. & Teng, M. W. L. Combination cancer immunotherapies tailored to the tumour microenvironment. *Nat. Rev. Clin. Oncol.* **13**, 143–158 (2016).
40. Bush, N. A. O., Chang, S. M. & Berger, M. S. Current and future strategies for treatment of glioma. *Neurosurgic. Rev.* **40**, 1–14 (2017).
41. Filippone, A. et al. PD1/PD-L1 immune checkpoint as a potential target for preventing brain tumor progression. *Cancer Immunol. Immunother.* **71**, 2067–2075 (2022).

Methods

Regulatory

Animal studies were performed in accordance with the protocols approved by the Institutional Animal Care and Use Committee (IACUC) at the University of Chicago (No. 72213) and the University of North Carolina at Chapel Hill (ID: 21-016.0).

Synthesis and characterization of ZnCDA and LipoCDA

ZnCDA particles were prepared in two steps. Briefly, an aqueous solution of CDA (0.2 ml, 5 mg ml^{-1}; Invivogen) and 0.15 M Na_3PO_4 was added to 5 ml of a mixture of 0.3 M Triton X-100 and 1.5 M 1-hexanol in cyclohexane and stirred vigorously for 15 min in the presence of DOPA (30 mg, 200 mg ml^{-1} in $CHCl_3$). An aqueous solution of $Zn(NO_3)_2$ (0.1 ml, 180 mg ml^{-1}) was added to 5 ml of a mixture of 0.3 M Triton X-100 and 1.5 M 1-hexanol in cyclohexane and stirred vigorously for 5 min. The $Zn(NO_3)_2$-containing microemulsion was added dropwise to the CDA-containing microemulsion and stirred vigorously for 30 min at room temperature. After the addition of 10 ml ethanol, the ZnCDA bare particles were obtained by centrifugation at 11,628 *g*. The resulting pellet was washed twice with tetrahydrofuran (THF)–ethanol and finally redispersed in THF. The ZnCDA NCP was prepared by adding a THF solution (80 µl) of DOPC, cholesterol and DSPE-PEG2000 (2:2:1) and the ZnCDA bare particles to 500 µl of 30% (v/v) ethanol–water at room temperature. The mixture was stirred at 600 *g* for 1 min. THF and ethanol were completely evaporated and the solution was allowed to cool to room temperature.

LipoCDA was prepared by mixing 100 µl 1,2-dioleoyl-3-trimethylammoniumpropane (DOTAP) (1 mg ml^{-1} in THF), 40 µl cholesterol (1 mg ml^{-1} in THF), 104 µl DSPE-PEG2000 (1 mg ml^{-1} in THF) and 1 mg CDA (5 mg ml^{-1}) followed by sonication in a water bath for 1 min and then transferred into a 10% ethanol aqueous solution. The organic solvents were removed under nitrogen gas.

Comparison of CDA dissociation and degradation in serum in vitro

First, 5 µg ml^{-1} CDA, LipoCDA or ZnCDA were dispersed in mouse plasma (collected from naïve mice) at 37 °C. At different time points, 20 µl aliquots of plasma were digested in 80 µl of 0.1 M HCl solution for 10 min followed by the addition of MeOH–acetonitrile (1:1). The solutions were cooled at 4 °C for 10 min, heated at 95 °C for 15 min and centrifuged for 10 min at 14,000 g. The supernatants were dried with nitrogen gas and resuspended in 50 µl of nuclease-free water and analysed by LC–MS.

In vivo drug pharmacokinetics and biodistribution analysis

C57BL/6 mice were intravenously (i.v.) injected with free CDA, LipoCDA or ZnCDA at an equivalent CDA dose of 10 µg. Plasma samples were collected at 5 min, 30 min, 1, 3, 5, 8, 24 and 48 hours post injection. For LC–MS detection, 20 µl plasma was digested in 80 µl of 0.1 M HCl solution for 10 min followed by the addition of 400 µl MeOH–acetonitrile (1:1). The solutions were cooled at 4 °C for 10 min, heated at 95 °C for 15 min and centrifuged for 10 min at 14,000 *g*. The supernatants were dried with nitrogen gas, resuspended in 50 µl of nuclease-free water and analysed by LC–MS. For analysis by enzyme-linked immunosorbent assay (ELISA), 20 µl plasma was digested in 80 µl of 0.1 M HCl solution for 10 min followed by ELISA analysis using a competitive ELISA kit (Cayman Chemical) according to the manufacturer's protocol.

Tumour-bearing mice were i.v. injected with ZnP-Pt and ZnCDA-Pt particles (with equal Pt content). Plasma, heart, brain, liver, lung, spleen, kidney and tumour samples were collected at 3, 8, 24, 48 and 72 hours post injection. The organs were weighed and the Pt concentrations quantified by ICP-MS.

Mice

C57BL/6 background mice were used in this study and wild-type mice were purchased from Envigo. *Tmem173*$^{-/-}$, *Ccr2*$^{-/-}$, *Ifnar1*$^{-/-}$, *Ifng*$^{-/-}$, OT-I CD8^{+} T-cell receptor (TCR), *LysM*^{cre}, *Tek*^{cre}, TRAMP and *Cd45.1* transgenic mice were purchased from the Jackson Laboratory. *Tmem173*$^{flox/flox}$ mice were kindly provided by J. Cambier of National Jewish Health. *Irf3*$^{-/-}$ mice were kindly provided by J. P. Y. Ting. For tumour studies, 6–8-week-old female mice were used in experiments with WT mice. For other studies using knockout or conditional knockout mice, the mice were 6–10 weeks of age and sex-matched in each experiment. For the TRAMP model, only 6-month-old male mice were used. All mice were housed in specific pathogen-free conditions: a 12-light/12-dark cycle was used, and temperatures of 20–23 °C with 30–70% humidity were maintained.

Cell lines and reagents

B16F10 (CRL-6475) and LLC (CRL-1642) cells were purchased from ATCC and were maintained according to the method of characterization used by ATCC. THP1-Dual KO-MyD reporter cells were purchased from InvivoGen (thpd-komyd) and were maintained according to the method of characterization. MC38 was a gift from Y.-X. Fu when he was working at the University of Chicago. GL261 was provided by B. Yamini of the University of Chicago in 2019. BL3750 was provided by H. Kohrt of Stanford University Medical Center in 2015. The stable STING knockdown cell line MC38$^{\Delta STING}$ was generated by D. R. E. Ranoa[42]. The stable IFNAR1 knockout cell line MC38$^{\Delta IFNAR1}$ was generated by C. Han by clustered regularly interspaced short palindromic repeats (CRISPR)–Cas9 with GTTGTAGTATGTTGACATTC as the guide RNA sequence. MC38-OVA-luciferase was a gift from S. Pitroda from University of Chicago. MC38-OVA and MC38-OT-I were selected as a single clone with 5 µg ml^{-1} of puromycin (InvivoGen) after stable infection with lentivirus expressing OVA or OT-I peptide. The cell lines were authenticated by western blot, flow cytometry and morphological analysis. Tumour cells were cultured in 5% CO_2 and maintained in DMEM medium (Corning) supplemented with 10% heat-inactivated fetal bovine serum (FBS; Sigma), 2 mM L-glutamine, 0.1 mM MEM non-essential amino acids, 100 U ml^{-1} penicillin and 100 µg ml^{-1} streptomycin. Anti-CD8α (2.43), anti-CD4 (GK1.5), anti-CSF1R (AFS98), anti-TNF-α (XT3.11), anti-IFNAR1 (MAR1-5A3), anti-IL-6R (15A7) and anti-PD-L1 (10F.9G2), and isotype antibodies rat IgG1 (TNP6A7), rat IgG2b (LTF-2), rat IgG2a (2A3) and mouse IgG1 (MOPC-21) were purchased from BioXcell. DiABZI and 2′3′-cGAM(PS)$_2$ (R_p/S_p) were purchased from InvivoGen.

Tumour growth and treatments

Tumour cells were subcutaneously injected into the backs of 8–10-week-old mice. For WT mice, 1×10^6 tumour cells were inoculated, for *Tmem173*$^{-/-}$, *Ifnar1*$^{-/-}$ and *Ifng*$^{-/-}$ mice, 5×10^5 tumour cells were inoculated, and for *Ccr2*$^{-/-}$ mice, 2×10^6 tumour cells were inoculated to keep tumours growing at a similar speed in the respective groups. The tumour volumes were measured along three orthogonal axes (*a*, *b* and *c*) and calculated as follows: tumour volume = $(a \times b \times c)/2$. Mice were euthanized before reaching the maximal tumour size (2,000 mm^3) approved by the IACUC of the University of Chicago. The mice were treated when the tumours reached an average volume of 120 mm^3 at around day 10–12 post tumour inoculation. In general, free CDA, ZnCDA, ZnP or LipoCDA at a considerable CDA dose of 10 µg was i.v. administered for a single dose, unless specified otherwise. Furthermore, 200 µg anti-CD8α (2.43), 200 µg anti-CD4 (GK1.5), 200 µg anti-PD-L1 (10F.9G2), 500 µg anti-TNF-α (XT3.11), 500 µg anti-IFNAR1 (MAR1-5A3), 300 µg anti-IL-6R (15A7) or the respective isotype control was injected intraperitoneally (i.p.) 1 day before treatment and every other day for three times in total; 100 µg anti-CSF1R (AFS98) or isotype control was injected i.p. daily three times before treatment and every other day post treatment (five times in total).

Establishment of the liver metastasis model

Mice were placed on a heating pad and anaesthetized with 3% isoflurane for induction and 2% for maintenance. Then, 70% ethanol was sprayed

on the abdomen or tail before surgery or injection. Mice were placed in the right lateral recumbent position. A 1-cm incision was made in the left upper abdominal wall followed by a 1-cm incision in the peritoneum to expose the spleen. Next, 5×10^6 MC38-OVA-luciferase cells in 50 µl PBS were gently injected into the spleen. The insertion site of the needle was cauterized and sealed with a GEMINI cautery (Braintree Scientific) to stem bleeding. Splenectomy was performed 5 min after injection using a GEMINI cautery. The abdominal incision was closed in two layers with 5-0 polydioxanone absorbable thread (AD Surgical). Mice were anaesthetized using the XGI-8 gas anaesthesia system (2% isoflurane; Xenogen). The fluorescence intensity was measured using the Lumina XR in vivo imaging system (Xenogen). Living Image (Ver.4.5, Xenogen) software was used to acquire an image sequence. The region of interest was drawn in the upper abdominal area and the photon flux data were measured.

Establishment of the orthotopic glioma model

Mice were anaesthetized by intraperitoneal injection of 90–120 mg ketamine and 5–10 mg xylazine per kg body weight. On reaching surgical tolerance, the mouse head was mounted onto a stereotaxic frame (David Instruments), the skull was exposed through a 5-mm longitudinal skin incision, and a hole was drilled 2-mm lateral (right) and 1-mm posterior to the bregma using a 25 G needle (BD PrecisionGlide). Using a stereotactically guided glass syringe (Hamilton), 2×10^5 GL261 cells were injected in 2 µl PBS to a depth of 3 mm from the dura surface into the right striatum. The injections were executed over a time period of 2 min, and the syringe was slowly withdrawn in three steps. The skin was closed using 5-0 polydioxanone absorbable thread (AD Surgical), and the mice were monitored on a heated pad until they regained consciousness. Tumour growth was monitored starting from day 7 post implantation by contrast-enhanced cone beam computed tomography (CT) once a week using a small X-rad 225Cx animal radiation research platform (Precision X-Ray). The mice were anaesthetized with 2–3% isoflurane in oxygen and positioned in the irradiator. Each mouse head was positioned in an anaesthesia nosecone, and CT scans were acquired with 360 projection images (1° per image) using X-ray tube settings of 60 kV and 0.8 mA and a 1.0 mm aluminium filter. To enhance soft tissue contrast, 300 µl Imeron-300 (equivalent to 90 mg iodine; Bracco) was i.v. injected 2 min before CT acquisition. ZnCDA or ZnP was i.v. administered at a considerable CDA dose of 10 µg once a week for three doses. The mice received 2 Gy whole-brain irradiation on days 8, 11 and 14 (in total 3 × 2 Gy). Tumour volumes were determined from cone beam CT scans using Horos software (v3.3.6, Horos Project).

Cytokine and chemokine detection

Mouse plasma and tumour tissues were collected 24 hours post ZnCDA treatment. The tumour tissues were weighed after collection, homogenized and centrifuged at 12,000 *g* for 10 min for supernatant collection. Protease inhibitor cocktails (Thermo Fisher) were added according to the manufacturer's protocol. Inflammatory cytokines and chemokines were measured using a LEGENDplex Mouse Inflammation Panel (13-plex) kit (Biolegend) according to the manufacturer's protocol.

Measurement of IFN-γ-secreting T cells by enzyme-linked immunosorbent spot assay

Tumour cells were collected and resuspended in RPMI 1640 medium supplemented with 10% FBS, 2 mM L-glutamine, 100 U ml^{-1} penicillin and 100 µg ml^{-1} streptomycin. $CD8^+$ or $CD4^+$ T cells were isolated using negative-selection sorting kits (STEMCELL). $CD11c^+$ DCs were sorted from naïve mice using STEMCELL kits. OVA (Sigma) or OT-I peptides (SIINFEKL; Invivogen) were added as repriming antigen at a concentration of 10 µg ml^{-1}. DCs and T cells were co-incubated for 48 hours at a ratio of 1:5 or 1:10. For TAM function detection, $CD8^+$ splenocytes from OT-I transgenic mice and $CD45^+CD11b^+F4/80^+Rho^+$ cells from treated tumours were purified using an AriaII cell sorter (BD Biosciences). A total of 2×10^5 to 4×10^5 $CD8^+$ cells were used in the assays. The ratio of TAMs to $CD8^+$ cells was 1:5 or 1:10. After 48 hours of incubation, the IFN-γ-secreting cells were determined with an IFN-γ enzyme-linked immunosorbent spot assay kit according to the manufacturer's protocol (BD Biosciences). The visualized cytokine spots were enumerated using an ImmunoSpot Analyzer (Cellular Technology).

Tumour-infiltrating T-cell blockade and tumour pre-existing T-cell depletion

FTY720 was purchased from Sigma-Aldrich. Mice were treated with FTY720 beginning either before (preFTY720) tumour inoculation or concurrently (postFTY720) with ZnCDA treatment to establish the role of pre-existing or infiltrating T cells. For preFTY720 blockade, 10 µg FTY720 was i.p. administered per mouse from tumour inoculation and every other day thereafter for five times. For postFTY720 blockade, 10 µg FTY720 was i.p. administered per mouse from 1 day before ZnCDA treatment and every other day thereafter for five times. For tumour pre-existing $CD8^+$ T-cell depletion, 50 µg anti-CD8α (2.43) or control antibodies were intratumourally injected from 1 day before ZnCDA treatment and every third day thereafter for three times.

BMDM generation and in vitro stimulation

Single-cell suspensions of bone marrow cells were obtained from the indicated mice, plated in 10-cm Petri dishes and cultured in culture medium (RPMI 1640 + 10% FBS + 20 ng ml^{-1} macrophage colony-stimulating factor (M-CSF)). Fresh culture medium was added on days 3 and 6. BMDMs were collected for stimulation assay on day 6. For in vitro stimulation, BMDMs were co-cultured with or without 1 or 10 µg ml^{-1} or an equal amount of CDA, ZnCDA or ZnP for 24 hours.

Generation of bone marrow chimeras

Tmem173$^{-/-}$ or WT mice were irradiated with a single dose of 10 Gy. The irradiated mice were adoptively transferred (i.v.) with 3×10^6 bone marrow cells from *Tmem173*$^{-/-}$ or WT donor mice on the same day. The mice were treated with neomycin (0.5 mg ml^{-1}) diluted in drinking water for 4 weeks after reconstitution. After approximately 8–10 weeks, the mice were used for tumour studies.

OVA uptake and degradation

WT, *Ifnar1*$^{-/-}$ or *Tmem173*$^{-/-}$ BMDMs were co-cultured with free CDA, ZnCDA and ZnP at a considerable CDA concentration of 1 µg ml^{-1} for 24 h. For the degradation assays, the supernatants were removed and the BMDMs were pulsed with DQ-OVA (Invitrogen) at 10 µg ml^{-1} at 37 °C for 15 min, washed twice, resuspended in complete media, monitored for up to 2 hours and placed on ice. For the uptake assays, the cells were incubated with 5 µg ml^{-1} OVA-AF647 (Invitrogen) at 37 °C and monitored for up to 2 hours. The uptake and degradation of OVA were calculated as the GMFI of OVA-AF647 or DQ-OVA, respectively, divided by the GMFI of the control (cells without OVA-AF647 or DQ-OVA).

Flow cytometry

Tumours were digested with 1 mg ml^{-1} collagenase IV (Sigma-Aldrich) and 200 µg ml^{-1} DNaseI (Sigma-Aldrich) at 37 °C for 30–60 min. For some experiments, cells were then pelleted by centrifugation at 400 *g* for 10 min and further purified with 40 and 70% Percoll (GE) solutions by centrifuging at 800 *g* (no brake) for 20 min at room temperature. Non-tumour cells were collected from the interface, and red blood cells were removed with lysis buffer. The following flow cytometry antibodies were used: CD16/CD32 (2.4G2) from BioXcell; CD45 (30-F11), CXCR5 (SPRCL5) and rat IgG2a,κ isotype (eBR2a) from eBioscience or Invitrogen; CD11b (M1/70), CD4 (RM4-5), CD8α (53-6.7), NK1.1 (PK136), CD3 (17A2), CD11c (N418), F4/80 (BM8), Ly6C (HK1.4), anti-MHCII (M5/114.15.2), MHCI (AF6-88.5), PD-1 (29F.1A12), CD80 (16-10A1), CD86 (GL-1), CD31 (390), PDPN (8.1.1), CD117 (2B8), CD127 (A7R34),

ST2 (D2H4), ICOS (7E.17G9), TCRg/d (GL3), Tim3 (RMT3-23), Ly108 (330-AJ), Ki67 (16A8), CD24 (M1/69), rat IgG2a,κ isotype (RTK2758), hamster IgG (HTK888), streptavidin and Lineage antibody mixture from BioLegend; Ly6G (1A8), NK1.1 (PK136), CD8 (53–6.7), F4/80 (T45-2342), TCF1 (S33-966) and CD11c (HL3) from BD Biosciences. Dead cells were excluded using LIVE/DEAD Fixable Yellow dead cell stain kit (Invitrogen). For staining 1×10^6 cells in a 100 µl volume, surface marker antibodies were used at 1:500 dilution (CD16/CD32 blocking antibody was used at 1:10,000, CXCR5 and Lineage antibody mixture was used at 1:100) and intracellular staining antibodies were used at 1:200 dilution. Flow cytometry was performed using a BD LSR Fortessa or a Cytek Aurora Red instrument, and the data were analysed with FlowJo (v10.8.1).

Histology and immunohistochemistry

Tissues were fixed with 4% paraformaldehyde for 2–3 days and sent to the university core facility for embedding and processing. The slides were stained with Leica Bond RX automated stainer. The protocol 'No post primary 1 h Bond DAB refine' was used. Epitope retrieval solution I (Leica Biosystems, AR9961) was used for heat treatment for 20 min. Primary rabbit monoclonal anti-mouse CD31 (Abcam, ab28364, 1:450) was used for 1 hour, and antigen–antibody binding was detected using Bond polymer refine detection (Leica Biosystems, DS9800). Slides were scanned using a CRi Pannoramic SCAN ×40 whole slide scanner and analysed with QuPath (v0.1.2) and ImageJ (v1.53a).

Bulk RNA-seq and analysis

Tumours treated with ZnP-Rho and ZnCDA-Rho were collected at 6 hours post treatment. Single cells were collected by digestion using 1 mg ml^{-1} collagenase IV (Sigma-Aldrich) and 200 µg ml^{-1} DNaseI (Sigma-Aldrich) at 37 °C for 30–60 min. $CD45^+CD11b^+F4/80^+Rho^+$ cells were purified using an AriaII cell sorter (BD Biosciences). RNA was extracted using TRIzol (Life Technologies) according to the manufacturer's instructions. The complementary DNA library was generated using a SMARTer Stranded Total RNA-Seq kit (v2, TaKaRa) according to the manufacturer's instructions. Libraries were validated with a 5200 Fragment Analyzer (Agilent) and quantified by quantitative PCR and Qubit fluorometric quantitation (Thermo Fisher). RNA-seq was performed by the genomics core facility at The University of Chicago using NovaSEQ6000 (Illumina). The raw sequencing data have been deposited in the National Center for Biotechnology Information database (Sequence Read Archive (SRA) accession no. PRJNA770747). RNA-seq analysis was performed on the Galaxy platform. Raw data quality control was performed using FastQC (ref. [43]). No samples were discarded from the analysis. Sequenced reads were aligned to mouse reference genome (mm10) with HISAT2 (ref. [44]), and the aligned reads were used to quantify messenger RNA expression using featureCounts[45]. The count data were further analysed for differential expression with limma-voom[46]. GSEA was performed with Hallmark or KEGG gene set collections of the Molecular Signature Database (https://www.gsea-msigdb.org/gsea/msigdb/index.jsp) using GSEA software (v4.1.0)[47]. The M1 polarization-associated gene set was generated according to a recent review[48].

Statistical analysis

For the tumour growth data, the descriptive statistics of tumour size were summarized by treatment group at each time point. Tumour growth curves were plotted over time by treatment group. Two-way ANOVA tests were used to analyse the tumour growth curves. For subcutaneous tumours, mice were taken off study when individual tumour volumes were ≥1,000 mm^3. For the metastasis, lymphoma and glioma models, mice were taken off study when moribund or found dead. The survival curves were analysed by Kaplan–Meier survival analysis using the log-rank (Mantel–Cox) test. Flow cytometry and T-cell function data were summarized, presented using descriptive statistics for each treatment and compared across treatment groups using two-way ANOVA or two-way Student's *t*-tests. Statistical figures were prepared using Excel (v16.63.1, Microsoft) and Prism software (v8.4.0, GraphPad).

Reporting summary

Further information on research design is available in the Nature Research Reporting Summary linked to this article.

Data availability

All data generated or analysed during this study are included in this published article and its Supplementary Information files. All raw sequencing data (SRA: PRJNA770747) are available online. The publicly available data used in this study are cited wherever relevant. Mouse reference genome (mm10): https://www.ncbi.nlm.nih.gov/grc/mouse; Molecular Signature Database: https://www.gsea-msigdb.org/gsea/msigdb/index.jsp.

References

42. Ranoa, D. R. E. et al. Molecular cell biology STING promotes homeostasis via regulation of cell proliferation and chromosomal stability. *Cancer Res.* **79**, 1465–1479 (2019).
43. Martin, M. Cutadapt removes adapter sequences from high-throughput sequencing reads. *EMBnet. J.* **17**, 10–12 (2011).
44. Kim, D., Paggi, J. M., Park, C., Bennett, C. & Salzberg, S. L. Graph-based genome alignment and genotyping with HISAT2 and HISAT-genotype. *Nat. Biotechnol.* **37**, 907–915 (2019).
45. Liao, Y., Smyth, G. K. & Shi, W. FeatureCounts: an efficient general purpose program for assigning sequence reads to genomic features. *Bioinformatics* https://doi.org/10.1093/bioinformatics/btt656 (2014).
46. Costa-Silva, J., Domingues, D. & Lopes, F. M. RNA-Seq differential expression analysis: an extended review and a software tool. *PLoS ONE* **12**, e0190152 (2017).
47. Subramanian, A. et al. Gene set enrichment analysis: a knowledge-based approach for interpreting genome-wide expression profiles. *Proc. Natl Acad. Sci. USA* **102**, 15545–15550 (2005).
48. Orecchioni, M., Ghosheh, Y., Pramod, A. B. & Ley, K. Macrophage polarization: different gene signatures in M1(Lps+) vs. classically and M2(LPS–) vs. alternatively activated macrophages. *Front. Immunol.* https://doi.org/10.3389/fimmu.2019.01084 (2019).

Acknowledgements

We are grateful to Z. Sun, A. Arina, S. P. Pitroda and T. Luo for helpful discussions, and R. Torres for technical assistance. We thank A. K. Huser for editing the manuscript. This work was supported by a grant from the Ludwig Foundation and an NIH grant (R01CA262508) to R.R.W., NIH grants (R01CA223184 and R01CA216436) to W.L. and NIH grants (R35CA232109 and R01AI141333) to J.P.Y.T. A.P. is the recipient of a Walter Benjamin scholarship provided by the German Research Foundation (Deutsche Forschungsgemeinschaft). J.B. was supported by a Clinical Therapeutics Training Grant (T32GM007019). We acknowledge the technical support from the University of Chicago Human Tissue Resource Center (RRID: SCR_019199), Animal Studies Core (P30CA014599), Microscopy Core (P30CA014599), Flow Cytometry Core (RRID: SCR_017760) and Mass Spectrometry Facility (CHE-1048528).

Author contributions

K.Y., W.H., W.L. and R.R.W. conceived the study; K.Y. designed the experiments; W.H. and X.J. prepared the nanoparticles; K.Y., W.H., X.J., A.P., C.H., S.L., Z.X., X.H., W.Z. and L.W. performed the experiments;

K.Y. and J.W. performed mouse genotyping; K.Y., W.H., X.J. and A.P. analysed the data; J.B., H.L., J.P.Y.T. and Y.-X.F. contributed resources; K.Y., J.B., W.L. and R.R.W. drafted and finalized the manuscript with input from all other authors.

Competing interests

R.R.W. has stock and other ownership interests with Boost Therapeutics, Immvira, Reflexion Pharmaceuticals, Coordination Pharmaceuticals, Magi Therapeutics and Oncosenescence. R.R.W. has served in a consulting or advisory role for Aettis, AstraZeneca, Coordination Pharmaceuticals, Genus, Merck Serono, Nano proteagen, NKMax America and Shuttle Pharmaceuticals. R.R.W. has a patent pending entitled 'Methods and kits for diagnosis and triage of patients with colorectal liver metastases' (US Patent application no. PCT/US2019/028071). R.R.W. has received research grant funding from Varian and Regeneron. R.R.W. has received compensation, including travel, accommodations or expense reimbursement, from AstraZeneca, Boehringer Ingelheim and Merck Serono. W.L. is the founder and chairman of Coordination Pharmaceuticals, which licensed the NCP technology from the University of Chicago. The other authors have no competing interests.

Additional information

Supplementary information The online version contains supplementary material available at https://doi.org/10.1038/s41565-022-01225-x.

Correspondence and requests for materials should be addressed to Wenbin Lin or Ralph R. Weichselbaum.

Peer review information *Nature Nanotechnology* thanks the anonymous reviewers for their contribution to the peer review of this work.